Materials and Design 186 (2020) 108203

Contents lists available at ScienceDirect

Materials and Design

journal homepage: www.elsevier.com/locate/matdes

The effect of heavy deformation on the precipitation in an Al-1.3Cu-1.0Mg-0.4Si wt.% alloy

Elisabeth Thronsen[a,*], Calin D. Marioara[b], Jonas K. Sunde[a], Kazuhiro Minakuchi[c], Tetsuya Katsumi[c], Iven Erga[d], Sigmund J. Andersen[b], Jesper Friis[b], Knut Marthinsen[d], Kenji Matsuda[e], Randi Holmestad[a]

[a]Department of Physics, Norwegian University of Science and Technology, Høgskoleringen 5, N-7491, Trondheim, Norway
[b]Materials and Nanotechnology Department, SINTEF Industry, Høgskoleringen 5, Trondheim, N-7465, Norway
[c]Machinery and Engineering Group, YKK Corporation, 200, Yoshida, Kurobe, Toyama, 938-8601, Japan
[d]Department of Materials Science and Engineering, Norwegian University of Science and Technology, Alfred Getz Vei 2, N-7491, Trondheim, Norway
[e]Graduate School of Science and Engineering for Research, University of Toyama, Toyama, 930-8555, Japan

HIGHLIGHTS

- An advanced TEM for detailed characterisation of precipitates in pre-deformed materials is presented.
- The effect of natural ageing and pre-deformation on precipitation in terms of type and distribution is investigated.
- The crystal structure of a previously reported phase in pre-deformed Al-Mg-Si(-Cu) alloys is presented.

GRAPHICAL ABSTRACT

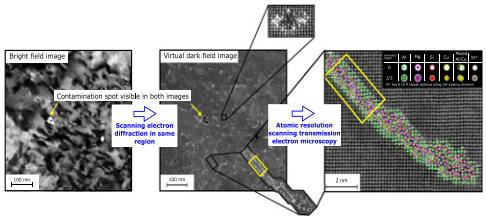

ARTICLE INFO

Article history:
Received 4 July 2019
Received in revised form 26 August 2019
Accepted 10 September 2019
Available online 24 October 2019

Keywords:
Al-Mg-Si-Cu alloys
Natural ageing
Pre-deformation
Precipitation
Scanning precession electron diffraction
High angle annular dark-field scanning transmission electron microscopy

ABSTRACT

This work has investigated the effect of the combination of natural ageing and 80% pre-deformation after solution heat treatment on precipitation during subsequent artificial ageing in an Al-1.3Cu-1.0Mg-0.4Si wt.% alloy. It was found that a combined use of atomic resolution aberration corrected high-angle annular dark-field scanning transmission electron microscopy and scanning precession electron diffraction enabled a detailed characterisation of precipitates in heavy pre-deformed materials. The dominant phase in the undeformed condition was the L phase. L was also found to be nucleated in the undistorted regions of the Al matrix in the pre-deformed conditions. Two phases with high aspect ratios were nucleated on dislocations: The C phase and a previously reported phase, which we named here the 'E phase'. The crystal structure of E was solved experimentally as monoclinic with core composition $Mg_6Al_2Si_2Cu_4$, supported by density functional theory calculations. It was determined that the order of pre-deformation and natural ageing had an influence on the relative fractions of the aforementioned phases formed during artificial ageing. An increased fraction of C+E relative to L was found in the condition where the pre-deformation was applied after natural ageing as compared to the condition where the pre-deformation was applied before natural ageing.

1. Introduction

Al-Mg-Si(-Cu) alloys are a class of materials with an increased use in the construction and automotive industries due to a combination

* Corresponding author.
E-mail address: elisabeth.thronsen@ntnu.no (E. Thronsen).

https://doi.org/10.1016/j.matdes.2019.108203

of desired properties such as light weight, high strength and good corrosion resistance. Their manufacturing consists of a succession of thermo-mechanical steps including casting, homogenisation, extrusion or rolling, solution heat treatment (SHT) and artificial aging (AA). The role of homogenisation is to reduce chemical segregation of the cast, and to produce dispersoidal AlSi(Mn,Fe) particles that will control grain size during the subsequent high temperature processing [1,2]. A solid solution is formed during SHT at temperatures above the solvus line of the system (>500 °C), consisting of a uniform dispersion of Mg, Si and Cu solute atoms substituting the Al positions in the FCC lattice, together with a high density of vacancies. This becomes super-saturated by rapid cooling, and constitutes the starting point of the AA, usually conducted at temperatures between 150°C and 200°C. During this process the solute atoms diffuse with the help of vacancies and form high numbers of nano-sized, metastable precipitates, which significantly affect the final properties of the material [3,4]. It is interesting to notice that with only 1 to 2 at.% added Mg, Si and Cu solute, the material can triple its strength during AA. The strength arises from the interaction between the dislocations and precipitates, since the precipitates effectively hinder the movement of dislocations in the matrix. The metastable precipitates have crystalline structures and form with different types, compositions, volume densities and size distributions, depending on the thermo-mechanical treatment of a given alloy. Therefore, the processing of the alloy is very important for the final properties.

In the Al-Mg-Si(-Cu) system, all the metastable phases have one main coherency direction with the Al matrix, along ⟨100⟩Al. In these directions the precipitates retain the FCC Al atomic arrangement, having atoms on two planes ($z = 0$ and $z = 0.203$ nm) with 0.405 nm repeat distance. Therefore, they grow with needle/rod/lath/plate morphologies along such directions and are viewed as projected atomic columns in cross-section in ⟨100⟩Al orientations. The precipitate development during AA from the super saturated solid solution (SSSS) and until the equilibrium phase forms is given as a precipitation sequence, which for the Al-Mg-Si-Cu system is [4]:

SSSS → solute clusters → GP zones →
β'', L → $\beta'_{(Cu)}$, L, S, C, Q′ → Q (Stable).

Solute clusters and Guinier-Preston (GP) zones are solute aggregates ordered on the FCC Al matrix positions. β'' is the main phase that forms in peak hardness conditions in the Al-Mg-Si alloys [3,5]. The phase has also been observed in Cu-added alloys, but here other Cu-containing precipitates such as L, S, C and Q′ become dominant with prolonged heating [4]. Cu is added to many Al-Mg-Si alloys because it improves hardness and thermal stability [4,6]. Analysis of the metastable precipitate crystal structures led to the realisation that they must be based on a similar sub-lattice with projected near-hexagonal symmetry of around 0.4 nm when viewed in cross-section [7]. It was later demonstrated that the sub-lattice is defined by Si atomic columns, and all the other atomic columns (Mg, Al, Cu) are located in-between [4,8]. This was called the 'Si-network'. It can take two different orientations in respect to the Al matrix. One orientation is defined by the Si network being aligned with ⟨310⟩Al, ⟨110⟩Al, ⟨510⟩Al and in the other the network is aligned with ⟨100⟩Al. The former is the most common and is present in all metastable precipitates in the Al-Mg-Si system, and in the S, β'_{Cu}, Q′ phases in the Al-Mg-Si-Cu system. The latter has only been found in the Cu-added alloys, in the L and C phases [4,9]. In the Al-Mg-Si-Cu system the Q′ phase is the metastable version of the equilibrium Q phase, being isostructural with it. It grows as laths with cross-section elongation along ⟨510⟩Al [4]. The C phase grows as a plate, with elongations along two ⟨100⟩Al directions [4,10]. β'_{Cu} is isostructural with the β'_{Ag} phase, with Cu replacing Ag in the structure, and is different from the β' phase in the Cu-free system [9,11]. The Q/Q′, C and β'_{Cu} phases are the only periodic structures so far reported in the Al-Mg-Si-Cu system. One characteristic of the Cu-added alloys is the formation of disordered structures which can be characterised by different orderings on the Si-network. It is common to observe several local ordered configurations of known phases in the same needle or lath, producing hybrid structures. In this respect the L phase is disordered and can contain local Q′ and/ or C phase parts, while S is also disordered and can contain Q′ and/ or β'_{Cu} parts [4]. In peak hardness conditions of such alloys it is also very common to observe hybrid precipitates containing β''/Q′/β'_{Cu} parts [12,13].

Another important milestone in the Al-Mg-Si(-Cu) system is the discovery of a set of construction rules for most precipitates, which arise from a line defect in the Al matrix [14]. According to these rules, every Al atom has 12 near neighbours, every Mg atom has 15 and every Si has 9. Interestingly, in precipitates Cu has 9 near neighbours as Si, and can take two different configurations, with columns in-between the Si network columns, or replacing 1/3 of the Si on the network. The former configuration is present in the Q′ and C phase, and the latter in the β'_{Cu} phase [9].

It has been shown that there are two processing steps that, introduced individually or in combination between SHT and AA, have an important influence on the subsequent precipitate development during AA and consequently on mechanical properties. These are storage at room temperature (RT) also known as natural ageing (NA), and pre-deformation. NA is important because the SSSS is unstable at RT. During this time atomic diffusion is taking place, leading to the formation of solute orderings and atomic clusters, with the effect of hardness increase and electrical conductivity decrease. For dense alloys with (Mg + Si >1 wt.%), the NA clusters have been found to have a negative effect on the precipitation of the hardening phases during the subsequent AA, causing a delay in precipitation and sometimes a reduction in the final hardness compared to when NA is avoided [15,16]. It has been found that the negative effect of natural ageing decreases with increasing Cu concentrations [17,18]. During AA treatment of a pre-deformed material, the dislocations act as heterogeneous nucleation sites for the precipitates. The deformation has a strong effect on the precipitation behaviour: The precipitate type, their microstructure and the local distribution are altered. It has been shown that in the distorted regions of the Al matrix, i.e. areas consisting of crystallographic defects associated with deformation like dislocations and subgrains, ' string-like' precipitates, along with smaller, elongated precipitate types and precipitates associated with over-ageing nucleate [19-22]. The faster coarsening of the precipitates nucleated on dislocations may be due to dislocations acting as short-circuit diffusion path for solutes during AA. Moreover, the introduction of dislocations prior to NA has been found to impede NA clustering [23,24]. The dislocations are believed to act as sinks for the quenched-in vacancies, thus suppressing the formation of NA clusters.

In addition to the conventional applications, novel usages are emerging for the Al-Mg-Si-Cu alloys. In the present work, a new Al-1.3Cu-1.0Mg-0.4Si wt.% intended for the zip fastener industry has been developed. The alloy's composition is listed in Table 1. The manufacturing process of these alloys consists of casting, homogenisation, extrusion, solution heat treatment (SHT), drawing, SHT and cold rolling corresponding to 80% deformation before the final artificial ageing (AA), see Fig. 1. A period of NA can be introduced before or after the cold rolling, which may affect the subsequent AA response. Given these facts, the main objectives of this work is to characterise the precipitates that form during AA in the heavily deformed materials, and to understand the effect of NA in connection to pre-deformation. Vickers hardness is measured at each processing step after the SHT, and hardness development is connected to precipitate microstructure. The microstructure of the alloy is investigated by the use of transmission electron microscopy (TEM). TEM is a powerful technique in visualising the precipitate distribution

Table 1
The measured composition of the alloy investigated in the present work.

	Cu	Mg	Si	Fe	Ti	B	Zn	Mn	Cr	Zr
wt.%	1.27	1.01	0.38	0.069	0.019	0.004	0.003	0.001	<0.001	<0.001

through conventional techniques, such as bright-field (BF) or dark-field (DF) imaging using diffraction contrast, and the precipitate structure through more advanced techniques providing atomic resolution such as high-angle annular dark-field scanning TEM (HAADF-STEM). Studying precipitation in heavily pre-deformed materials by conventional techniques however, is challenging due to the contrast from dislocations masking out the precipitates.

Recently, scanning precession electron diffraction (SPED) has emerged as a promising technique in quantifying the precipitates in undeformed Al alloys [25,26]. By means of this technique, one may form virtual dark-field images using the 4D data set that comprised a 2D PED pattern in each pixel of a 2D scan area. The benefit of this technique is the acquisition of large data-sets that enable detailed statistical characterisation of microstructure, providing location, type and size for a large number of precipitates. In this study we will evaluate the applicability of SPED on heavily deformed Al alloys, as well as quantitatively explain the difference in deforming prior to- or after NA based on material hardness and precipitation.

2. Experimental procedure

2.1. Material and heat treatment

The alloy was cast, homogenised (505°C, 3 h), extruded and solution heat treated (505°C, 3 h) before drawing. Cylindrical bars (Ø 3.8 mm) were subjected to SHT at 505°C for 3 h and subsequently water quenched to room temperature. Three different conditions abbreviated 'NA20ha', 'NA20hb' and 'NA20hn' were investigated in the present work, see Fig. 1. For condition NA20ha, SHT was succeeded by NA for 20 h, followed by 80 % cold rolling and AA at 170°C for 3 h. NA20hb was cold rolled to 80 % immediately after SHT, followed by 20 h NA and subsequent AA at 170 °C for 3 h. NA20hn was exposed to 20 h NA followed by AA for 3 h at 170 °C without any deformation.

2.2. Vickers hardness tests

Prior to Vickers hardness tests, all samples were polished with a Saphir 330 equipped with grinding plates with grit sizes from 120 up to 4000 P. A Zwick/Roell ZHV30 indent machine equipped with JS-Tango controller unit was used for hardness measurements. For the undeformed and deformed samples, a total of 9 and 10 indentations were used per condition, respectively.

2.3. TEM sample preparation

TEM samples were prepared by first mechanically polishing the material down to 100 µm thickness using a Struers Rotopol-21. 3 mm diameter discs were then punched out normal to the drawing direction for the undeformed condition and normal to the rolling direction for the pre-deformed conditions. Subsequently, the samples were electropolished by using a Struers TenuPol-5 with an applied voltage of 20 V for the deformed samples and 14.6 V for the undeformed sample. The electrolyte was kept at a temperature of −25 ± 5°C and consisted of 1/3 nitric acid and 2/3 methanol. In order to reduce the risk of carbon contamination build-up under the data acquisition during SPED and HAADF-STEM investigations, the specimens were cleaned using a Fischione 1020 Plasma Cleaner before insertion into the TEM.

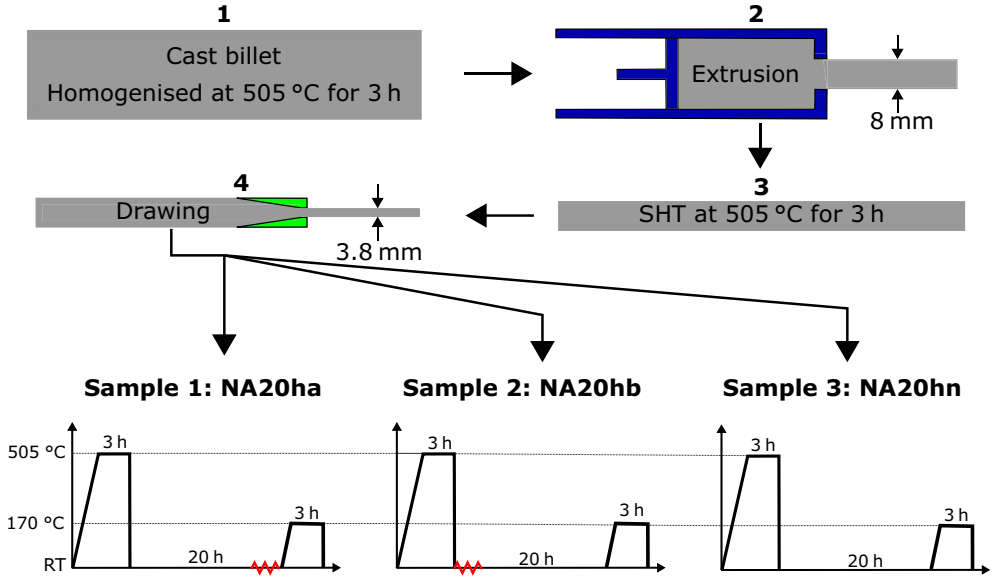

Fig. 1. The material processing prior to the as-received condition is shown in steps 1–4, along with the subsequent processing of the three different samples NA20ha, NA20hb and NA20hn. Both NA20ha and NA20hb were deformed by cold rolling to 0.76 mm, corresponding to 80% deformation.

2.4. TEM studies

A JEOL 2100F operated at high voltage of 200 kV and equipped with a NanoMEGAS ASTAR system was used to acquire the SPED scans. The PED patterns were collected by mounting an Allied Vision Stingray camera in the binocular stand outside the microscope column. While performing SPED, the instrument was operated in nanobeam diffraction mode using an unprecessed probe diameter of about 1.3 nm and semi-convergence angle $\alpha \approx 1$ mrad. The employed precession angle and corresponding precession frequency was kept at 1.0° and 100 Hz, respectively. The exposure time was set to 40 ms per pixel and the scan step size was 1.52 nm. The alignment of the precessing electron beam was done in accordance with the procedure reported by Barnard et al. [27]. In addition, the JEOL 2100F was used to acquire BF images.

The acquisition of the high resolution HAADF-STEM images was done in a double (image and probe) corrected JEOL ARM200F operated at 200 kV. The following parameters were used to obtain the images: 0.08 nm probe size, a semi convergence angle of 28 mrad, the inner and outer collection angles were 35 and 150 mrad, respectively. The inner collection angle is somewhat smaller than what is considered optimal for HAADF-STEM (50 mrad), but our experience is that the lower Z-contrast Mg-containing atomic columns are better resolved with this setting. When imaging in an ⟨100⟩ zone axis of Al, this technique provides atomic resolution of precipitates atomic columns along their main coherency direction with the Al matrix, having Z-contrast. Based on such images, the crystal structures of individual precipitates can be identified and presented as atomic overlays. The atomic overlay is made according to the construction rules for precipitates in the Al-Mg-Si(-Cu) system [14] mentioned in the introduction, which imply that in the overlay every Al atom is surrounded by four atoms of opposite height, every Mg by five and every Si and Cu by three.

Atomic resolution HAADF-STEM images in general have low signal-to-noise ratio. To improve clarity, all of the HAADF-STEM images shown in this paper are filtered using a circular bandpass mask applied on the respective fast fourier transform (FFT), and an inverse FFT (IFFT) was performed on the masked area, suppressing all features with separation shorter than 0.15 nm in real space. It should be noted that 0.15 nm is close to the minimum projected atomic column separation for precipitates in the Al-Mg-Si(-Cu) system viewed along their needle lengths.

2.5. Density functional theory calculations

The density functional theory (DFT) calculations were performed with the Vienna ab initio simulation package (VASP) [28,29] using the projector augmented wave method (PAW) within the PBE (Perdew-Burke-Ernzerhof) generalised gradient approximation [30]. The plane wave energy cutoff was 400 eV. For all calculations, gamma-centred k-points were used with a maximal k-point distances of 0.18 $Å^{-1}$ in each direction. The electronic accuracy for self-consistent loops was set at 10^{-6} eV. The atomic positions were relaxed to a maximum force of 0.001 ev $Å^{-1}$ between atoms, using 1st order Methfessel-Paxton for smearing of partial occupation and a smearing factor of 0.2. For accurate energies, a separate calculation was performed using the tetrahedron method with Blöchl correction for the smearing. The formation enthalpies were calculated according to Ref. [31] with solid solution reference energies E_x obtained from a 4×4×4 Al supercell with 255 Al atoms and a single solute atom X, X=Al, Mg, Si, Cu.

2.6. SPED data analysis

SPED involves rastering a precessing, nanometre-sized electron probe over an area of interest and recording the transmitted diffraction pattern at each probe position [27]. The net result is a 4D data set that comprised a 2D PED pattern at each position of a 2D area scan. The 4D SPED data sets were processed using the open-source Python library HyperSpy [32]. The source code used in the present work is developed by Sunde et al. and a thorough review can be found in [26]. A short summary is given here:

1. A *virtual aperture* is placed in the obtained PED pattern stack and the image intensity within the aperture is integrated. The value obtained is used to assign a colour-scale tone to the pattern's corresponding real-space position, resulting in the formation of a virtual dark-field (VDF) image after running through the full stack.
2. A real space *navigation mask* is created by masking out precipitate-free areas in the VDF.
3. A reciprocal space *signal mask* is created by masking out the Al reflections using a bulk Al PED pattern.
4. An unsupervised machine learning approach based on non-negative matrix factorisation (NMF) is applied to the SPED scan data highlighted by the constructed masks.

The NMF decomposition returned *component patterns* representing the data in reciprocal space, resembling PED patterns of specific features such as different precipitate types, in addition to the corresponding *loadings* at each pixel in real space. The *loading maps* indicate where the associated component patterns are significant and resemble simplified dark field images [33]. In theory, the number of components should equal the number of unique phases present multiplied by the number of allowed orientations. However, due to imperfections of the scans, such as bending across the strain area, imperfect masks, strain, a larger amount of components had to be included. By trial-and-error, a total number of 40 and 90 components for NA20ha and NA20hb, respectively, was found to adequately represent the features of interest in the SPED data.

Through comparison with the FFTs of previously obtained HAADF-STEM images, the component patterns were categorised. Components which did not match any of the FFTs were categorised as disordered, based on the HAADF-STEM images. Once identified, the real-space intensities of the components corresponding to the same precipitate were normalised and summed up. The net result yields a simplified and reconstructed description of the diffraction data, showing where each precipitate type is located in the scan area. Finally, precipitate phase fractions were estimated using a pixel-based calculation where the sum of pixels associated with one precipitate type was divided by the total number of pixels representing all the precipitate types.

Through comparison with the FFTs of previously obtained HAADF-STEM images, the component patterns were categorised. Components which did not match any of the FFTs were categorised as disordered, based on the HAADF-STEM images. Once identified, the real-space intensities of the components corresponding to the same precipitate were normalised and summed up. The net result yields a simplified and reconstructed description of the diffraction data, showing where each precipitate type is located in the scan area. Finally, precipitate phase fractions were estimated using a pixel-based calculation where the sum of pixels associated with one precipitate type was divided by the total number of pixels representing all the precipitate types.

A short summary is given here:

1. A *virtual aperture* is placed in the obtained PED pattern stack and the image intensity within the aperture is integrated. The value obtained is used to assign a colour-scale tone to the pattern's corresponding real-space position, resulting in the formation of a virtual dark-field (VDF) image after running through the full stack.

2. A real space *navigation mask* is created by masking out precipitate-free areas in the VDF.
3. A reciprocal space *signal mask* is created by masking out the Al reflections using a bulk Al PED pattern.
4. An unsupervised machine learning approach based on non-negative matrix factorisation (NMF) is applied to the SPED scan data highlighted by the constructed masks.

The NMF decomposition returned *component patterns* representing the data in reciprocal space, resembling PED patterns of specific features such as different precipitate types, in addition to the corresponding *loadings* at each pixel in real space. The *loading maps* indicate where the associated component patterns are significant and resemble simplified dark field images [33]. In theory, the number of components should equal the number of unique phases present multiplied by the number of allowed orientations. However, due to imperfections of the scans, such as bending across the strain area, imperfect masks, strain, a larger amount of components had to be included. By trial-and-error, a total number of 40 and 90 components for NA20ha and NA20hb, respectively, was found to adequately represent the features of interest in the SPED data.

Through comparison with the FFTs of previously obtained HAADF-STEM images, the component patterns were categorised. Components which did not match any of the FFTs were categorised as disordered, based on the HAADF-STEM images. Once identified, the real-space intensities of the components corresponding to the same precipitate were normalised and summed up. The net result yields a simplified and reconstructed description of the diffraction data, showing where each precipitate type is located in the scan area. Finally, precipitate phase fractions were estimated using a pixel-based calculation where the sum of pixels associated with one precipitate type was divided by the total number of pixels representing all the precipitate types.

3. Results and discussion

3.1. The influence of deformation and natural ageing on hardness evolution

The hardness response during NA for a sample deformed immediately after quenching from the SHT temperature and a undeformed sample is shown in Fig. 2a. The AA response for NA20ha, NA20hb and NA20hn at 170°C is shown in Fig. 2b, while Fig. 2c–e shows the hardness response during all processing steps after SHT for NA20ha, NA20hb and NA20hn, respectively, up until the conditions chosen for the TEM samples. In (a), the dashed, vertical line marks the point where the NA time is 20 h, while in (b) it indicates the condition of the samples prepared for TEM which corresponds to the maximum hardness of NA20hb, obtained after around 3 h. NA20ha reaches its maximum hardness after 6 h, while the undeformed sample, NA20hn, does not reach peak hardness after the maximum investigated time, 10 h. This suggests that the introduced dislocations enhance the precipitation kinetics, thereby shortening the AA time required to obtain the peak age condition.

The hardness response during NA is enhanced for the undeformed samples as compared to the pre-deformed samples, see Fig.2a, c and d. After 20 h the increase in hardness is 9 HV and 12 HV for the pre-deformed and undeformed samples, respectively. This is believed to be caused by reduced NA response in the pre-deformed samples due to vacancy annihilation at the dislocations [34,35]. The overall increase in hardness during NA of the pre-deformed sample throughout the measurement times is 10 HV, i.e. the hardness increase from 20 h NA time to five days NA time is only 1 HV, see Fig. 2a.

The pre-deformed samples obtain higher hardness than the undeformed sample for all measured AA times. By comparing Fig. 2c, d and e, it can be seen that the introduction of dislocations through the cold deformation prior to AA is responsible for the difference, and in the same time the contribution to hardness from precipitates is lower

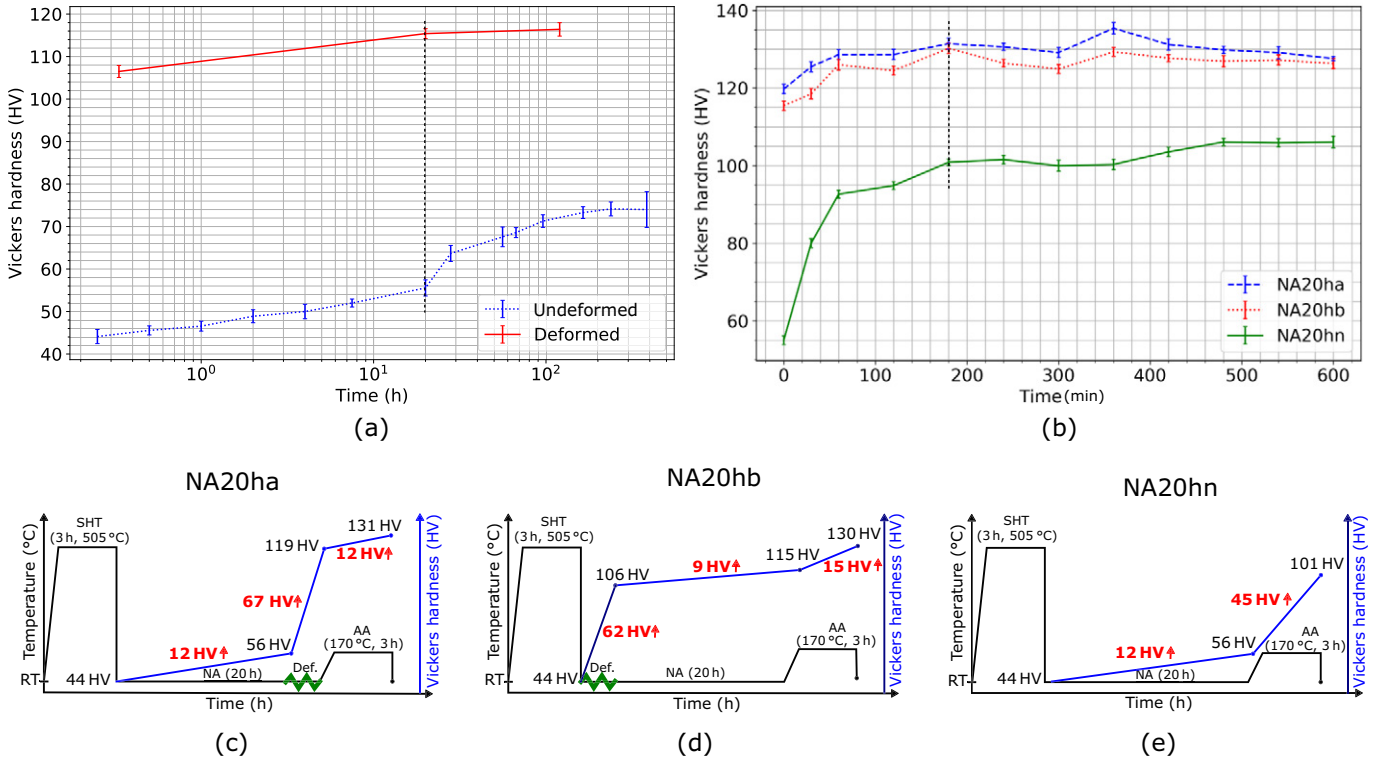

Fig. 2. In (a) the hardness evolution during NA for a pre-deformed and a undeformed sample is displayed. (b) Shows the AA response at 170 °C for the samples. It can be seen that NA20ha and NA20hb reach maximum hardness after 6 h and 3 h, respectively, while NA20hn does not reach peak age after 10 h. In (c), (d) and (e), the hardness increase associated with each processing step after solution heat treatment is shown for NA20ha, NA20hb and NA20hn, respectively.

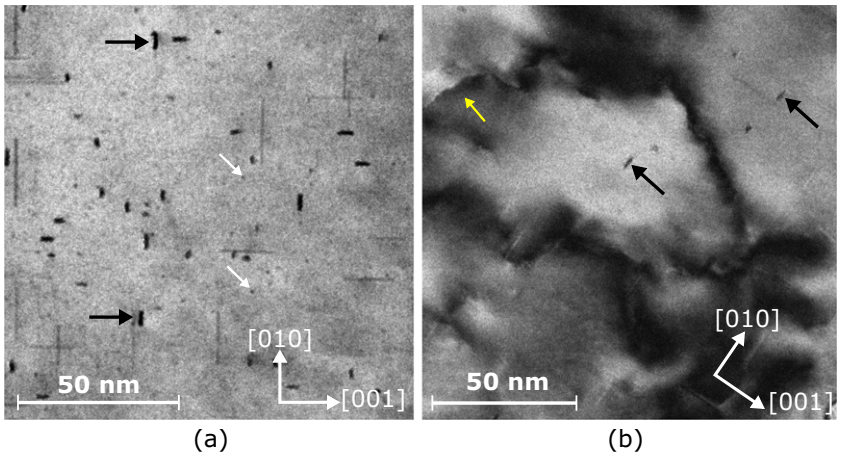

Fig. 3. (a) BF image showing the precipitate distribution in condition NA20hn. The black arrows indicate lath shaped precipitates with habit plane $\{100\}_{Al}$, while the white arrows indicate significantly smaller, rod shaped precipitates. (b) BF image showing the microstructure of one of the pre-deformed samples. The black arrows indicate precipitation in undistorted regions and the yellow arrow indicates a dislocation line.

in the pre-deformed conditions as compared to the undeformed. Moreover, pre-deformation after NA (NA20ha) gives a slightly harder sample after AA. For AA times exceeding 600 min the curves of the two pre-deformed samples are starting to coincide. This may suggest that a fraction of the precipitates in NA20ha are less thermally stable or that the dislocation density in this state is decreasing more rapidly than in NA20hb.

3.2. Precipitate distribution and microstructure of the undeformed sample

Fig. 3a and b shows BF images obtained in $\langle 100 \rangle_{Al}$ orientation for condition NA20hn and NA20ha. For the undeformed sample, the microstructure consists of two main types of precipitates, indicated by the white and black arrows. The precipitates indicated by the black arrows have habit plane $\{100\}_{Al}$ and are lath shaped, while the precipitates indicated by the white arrows are much smaller and are shaped as rods. In the pre-deformed sample (NA20ha), it is observed that precipitates are nucleated in the undistorted regions of the Al matrix, exemplified by the black arrows. The yellow arrow in (b) indicates the presence of a dislocation line. Due to the strong contrast from the dislocations in this and similar images, it is not possible to state if the dislocations are decorated by precipitates or not. Based on the results presented in the following subsections, precipitates are indeed found to decorate dislocations in the pre-deformed conditions. BF imaging was thus deemed unsuitable for visualising the precipitate distribution in the pre-deformed samples.

Fig. 4 shows an HAADF-STEM image of the precipitate microstructure for the undeformed sample. Based on such images, the lath shaped precipitates in Fig. 3a were found to be L phases. One example of the L phase is shown to the left in Fig. 4. The precipitates with very small cross-sections indicated by the white arrows in Fig. 3a were found to be structural units of GPB zones, indicated by white arrows in Fig. 4. GPB zones belong to the Al-Cu-Mg alloy system and are believed to form during the initial stages of AA [36,37].

3.3. Precipitate microstructure of the pre-deformed samples

The first part of the microstructure investigation of the pre-deformed samples involves analysis of precipitate crystal structures by HAADF-STEM. All images presented in the following are taken in a $\langle 100 \rangle_{Al}$ orientation. It is observed that precipitates nucleate in the distorted regions of the Al matrix, as well as in undistorted regions away from the dislocation network. Some regions of the images are atomically overlaid and the legend is presented in Fig. 5.

A representative selection of precipitates found in the pre-deformed conditions is shown in Fig. 6. The C phase was found to nucleate in the distorted regions of the Al matrix, one example is given in Fig. 6a through c, where three images of the same structure are shown. The numbered regions indicate distinguishable segments of the structure. Regions (1) and (4) indicate disordered parts of the structure. Region (2) indicates a segment of the structure nucleated in the C phase configuration. Likewise, the segment in region (5) is nucleated in the C phase configuration. However, whereas in region (2) the C phase is viewed along the $[001]_C$ direction, the segment in (5) is viewed along the $[010]_C$ direction. The C phase was first reported by Marioara et al. [4] and the structure was later solved by Torsæter et al. [10]. The crystal structure of this phase used in the atomic overlay in Fig. 5 is given in Table 2 and is derived from Ref. [10]. It is interesting to notice that peripheral alternating Si-Mg atoms in the C phase unit cell become Al (marked by white arrows) and constitute the $\{100\}_{Al}$ interface. The region in (3) consists of a periodic structure with habit plane $\{110\}_{Al}$ and 0.86 nm periodicity along $\langle 110 \rangle$Al. It is previously reported [21], but the structure has not been solved until now. We name it here the 'E phase', and discuss it in detail in the following subsection.

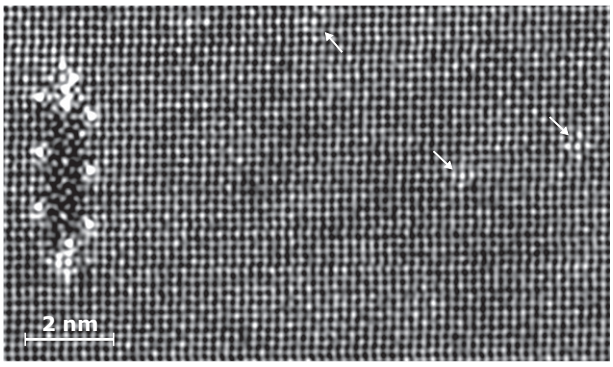

Fig. 4. HAADF-STEM image of NA20hn showing structural units of GPB zones indicated by white arrows, in addition to one example of the lath shaped L phase on the left hand side.

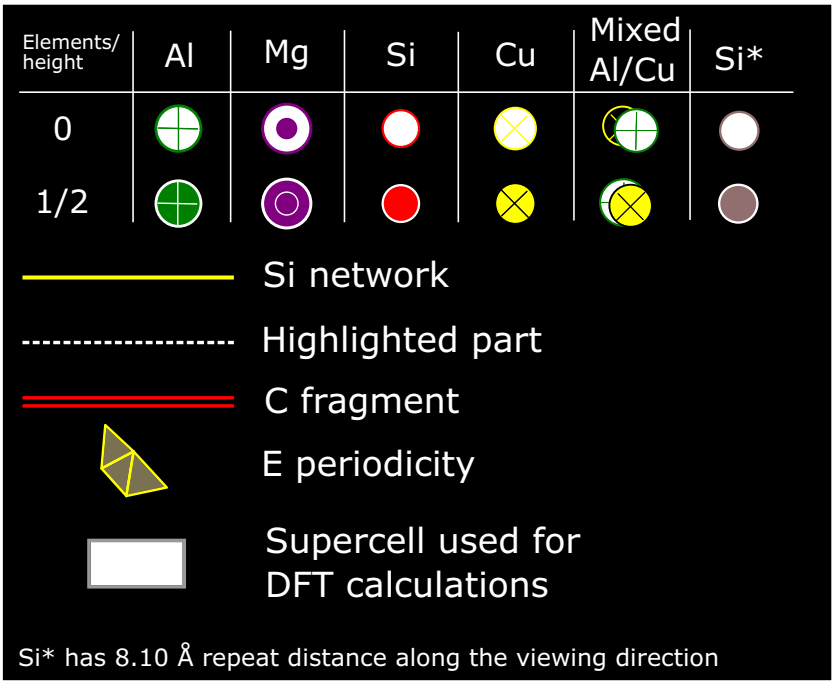

Fig. 5. Legend representing the overlays of HAADF-STEM images in the following subsections.

Precipitate structures like the one shown in Fig. 6a–c were found for both pre-deformed conditions, often consisting of two or more C phases connected by either disordered parts or short segments of the E phase. Furthermore, precipitates like the one imaged in (d) were also found to nucleate in the distorted regions of the Al matrix. The precipitates in Fig. 6a–d resembles the string-type reported in previous work on pre-deformed Al-Mg-Si alloys by Matsuda et al. [19,20] and more recently by Saito et al. [12,38], in the latter case for Al-Mg-Si-Cu alloys. The string-like precipitates like the one shown in (d) consists of segments of E type precipitates connected by disordered parts categorised as S phases. The precipitate in Fig. 6a–c may also be categorised as the string-type. This may imply that the C and E phases are ordered versions of the string-type. Discrete, disordered precipitates were also found to nucleate in the distorted regions of the Al matrix, one example is shown in (e) along with the corresponding FFT. The precipitate has habit plane $\{100\}_{Al}$, thus it can be categorised as an L phase. Discrete L precipitates nucleated in the distorted regions of the Al matrix were not found to be common based on the HAADF-STEM images, but were rather found to connect with or reside nearby larger structures.

As mentioned in the Introduction, there exist a nearly hexagonal sub-lattice known as the Si-network in all precipitate phases in the Al-Mg-Si(-Cu) system. The projected separation of the Si-network is $a \approx 0.4\,\text{nm}$. Therefore, in FFT patterns it corresponds to spots having $2.89\,\text{nm}^{-1}$ and $5\,\text{nm}^{-1}$ spatial frequencies. These spots are easily identifiable, even in the case of disordered precipitates. In the FFTs presented in Fig. 6e–g, only spots corresponding to the $5\,\text{nm}^{-1}$ spatial frequencies are connected by yellow lines.

Based on 53 and 69 HAADF-STEM images taken from the NA20ha and NA20hb conditions, respectively, it was concluded that the same precipitate types nucleate in the distorted regions of the Al matrix in both pre-deformed conditions. It is proposed that the underlying mechanisms governing the precipitation in such areas are independent of whether the deformation is applied prior to- or after NA.

Analysis of the 53 images obtained for NA20ha concluded that only one type of precipitate nucleates in the undistorted regions of the Al matrix: the L phase. One example is shown in Fig. 6f, along with the corresponding FFT. The L phase was found to nucleate in undistorted regions in NA20hb as well, however an additional category of precipitates was found here. One example is shown in Fig. 6 g, along with the corresponding FFT. The yellow lines indicate part of the Si-network. Such phases were disordered, but due to Cu incorporation and $\{130\}_{Al}$ habit plane, they can be categorised as the S phase [4].

3.4. Crystal structure of the E phase

As previously mentioned, the E phase was observed in both the NA20ha and NA20hb conditions. It has habit plane $\{110\}_{Al}$ and a periodicity of 0.86 nm along $\langle 110\rangle$Al. The E phase may be important for the material properties in pre-deformed Al-Mg-Si(-Cu) as it is seen to decorate dislocation lines and to connect more disordered precipitate-types along dislocation lines. The phase was first reported by Teichmann et al. [21] which studied the effect of 10% pre-deformation in an Al-Mg-Si alloy. However, the images recorded in that work were in high resolution TEM (HRTEM) mode with insufficient resolution to solve the structure. Fig. 7 shows an FFT filtered HAADF-STEM image of a precipitate with local arrangements of the E phase. The Z-contrast reveals a strong enrichment of Cu at the interfaces. The phase periodicity is indicated by the semi-transparent yellow areas.

As a first step in solving the crystal structure of the E phase, Fig. 7 was atomically overlaid based on the construction rules mentioned in the Introduction, the result is shown in Fig. 8a. The Si-network was found to be fragmented into three parts, indicated by the numbers. The longest segment exhibiting the E-phase periodicity is the lower part (no. 3). The Burger's vector $\vec{b}$ indicates the presence of a screw dislocation, believed to be the nucleation site of the precipitate. A supercell comprising Al and the core of the E phase was

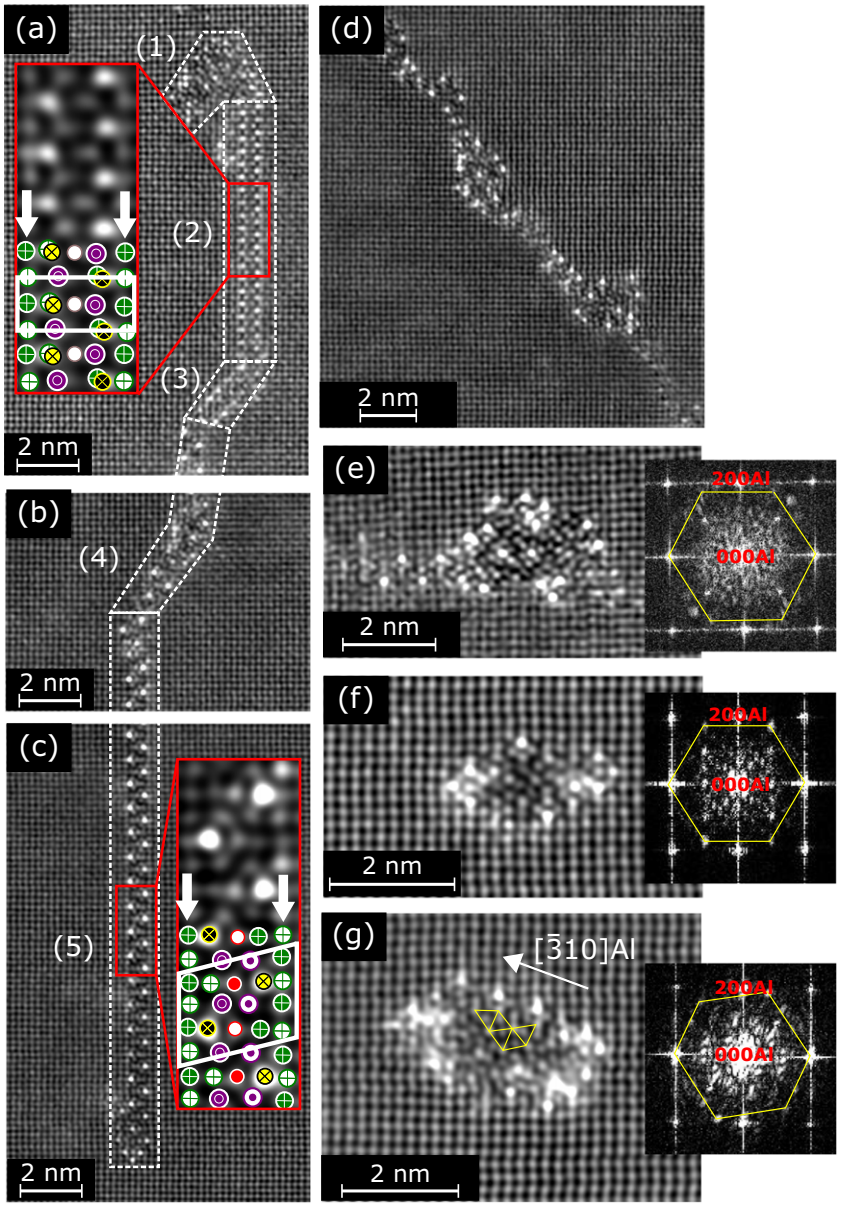

Fig. 6. FFT filtered HAADF-STEM images of different precipitate structures found in the pre-deformed samples. (a)–(c) Different part of the same precipitate. The regions enclosed by dotted lines represent different segments with different ordering in the precipitate. Parts of region (2) and (5), which show two different orientations of the C phase, are atomically overlaid and the unit cells are indicated by the white lines. (d) and (e) show two different types of precipitate nucleated in the distorted parts of the Al matrix. (f) and (g) are examples of precipitate nucleated in the undistorted parts of the Al matrix, categorised as L phase and S phase, respectively. The latter was only observed in NA20hb. In (e)–(g) the FFTs of the images are included.

extracted based on the image and is shown in (b). The black lines indicate the core of the precipitate. The supercell has dimensions $a = 24.34$Å$, b = 4.05$Å$, c = 8.59$Å, and all angles near 90°. However, the highest symmetry for the extracted atomic coordinates was $P2_1$ (space group 4) and thus we propose a monoclinic unit cell for the E phase.

Interestingly, structural similarities are found between the core of the E phase (b) and the core of the C phase (c). The interfacial atoms, denoted by (1) in both (b) and (c), differ: The Si atoms at the interface of the C phase are replaced by Cu atoms in the E phase. Moreover, the atoms within the core, denoted by (2), which in the C phase are Cu atoms, are replaced by Al atoms in the E phase. Some of the atoms are in addition shifted slightly in the E phase compared to the atoms' position in the C phase.

DFT calculations based on three different models of the E phase were employed. The first supercell, based on the experimental findings in this work has $Al_{38}Mg_6Si_2Cu_4$ composition and is shown in Fig. 8b. Based on the fact that the precipitate also has been reported in alloys without Cu, a Cu-free variant where the Cu atoms (denoted (1)) in Fig. 8b) at the interface were replaced by Si atoms, was also utilised. This variant has the composition $Al_{38}Mg_6Si_6$. Due to the observation of the similarities between the core of the E phase with the core of the C phase, a variant where the interfacial Cu atoms denoted (1) in Fig. 8b were replaced by Si atoms and the Al atoms denoted (2) in Fig. 8b were replaced by Cu atoms was also modelled. The latter has composition $Al_{36}Mg_6Si_6Cu_2$.

The results from the DFT calculations are shown in Table 3. According to the calculations, the model based on the experimental

Table 2
The atomic models for the C phase and the E phase. The space group of both phases is the monoclinic $P2_1$ (no. 4). The model for the C phase is derived from Ref. [10], while the model for the E phase is based on the DFT model exhibiting the lowest formation enthalpy (see Table 3).

C phase				E phase[1]		
$a_C = 10.32$ Å, $b_C = 4.05$ Å, $c_C = 8.10$ Å $\alpha_C = 90°, \beta_C = 100.9°, \gamma_C = 90°$				$a_E = 24.43$ Å, $b_E = 3.98$ Å, $c_E = 8.59$ Å $\alpha_E = 90°, \beta_E = 90°, \gamma_E = 90°$		
Atom	**x**	**y**	**z**	**x**	**y**	**z**
Al	–	–	–	0.148	0.250	0.085
Al	–	–	–	0.148	0.250	0.416
Al	–	–	–	0.147	0.250	0.750
Al	–	–	–	0.791	0.250	0.750
Al	–	–	–	0.793	0.250	0.418
Al	–	–	–	0.793	0.250	0.082
Al	–	–	–	0.266	0.250	0.085
Al	–	–	–	0.266	0.250	0.416
Al	–	–	–	0.263	0.250	0.750
Al	–	–	–	0.675	0.250	0.410
Al	–	–	–	0.675	0.250	0.089
Al	–	–	–	0.386	0.250	0.750
Al	–	–	–	0.443	0.250	0.250
Al	–	–	–	0.030	0.250	0.085
Al	–	–	–	0.030	0.250	0.416
Al	–	–	–	0.029	0.250	0.750
Al	–	–	–	0.089	0.750	0.583
Al	–	–	–	0.970	0.750	0.915
Al	–	–	–	0.970	0.750	0.584
Al	–	–	–	0.971	0.750	0.250
Al	–	–	–	0.911	0.250	0.750
Al	–	–	–	0.911	0.250	0.417
Al	0.680	0.500	0.810	0.911	0.250	0.082
Si	0.500	0.500	0.250	0.491	0.250	0.750
Si	0.830	0.500	0.080	–	–	–
Si	0.830	0.500	0.580	–	–	–
Mg	0.610	0.000	0.030	0.656	0.250	0.750
Mg	0.610	0.000	0.530	0.553	0.250	0.470
Mg	0.940	0.000	0.360	0.553	0.250	0.030
Mg	0.940	0.000	0.860	–	–	–
Cu	0.680	0.500	0.310	0.370	0.250	0.043
Cu	–	–	–	0.370	0.250	0.458

[1] The angles of the E phase is based on the DFT supercell. The unit cells angles may be approximately 90 degrees, but the atoms order in a $P2_1$ symmetry and no orthorombic space group was found for the precipitate phase.

observations, $Al_{38}Mg_6Si_2Cu_4$, is most energetically favourable, indicating that Cu must stabilise the Cu-free variant observed in the work of Teichmann et al. [21]. The refined fractional coordinates of the atomic sites in the energetically favourable model are shown in Table 2.

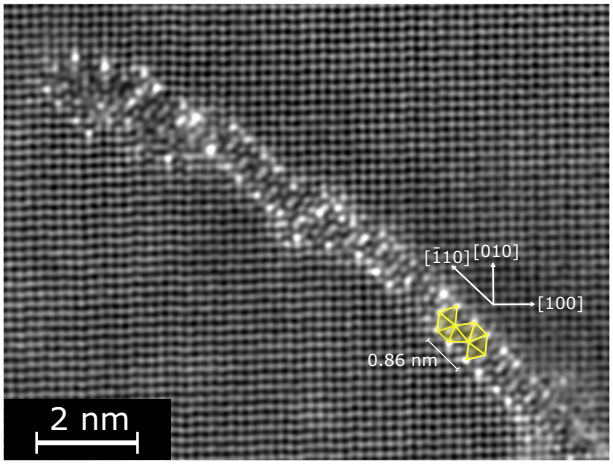

Fig. 7. FFT filtered HAADF-STEM image of one of the precipitate structures found in the pre-deformed samples. Parts of the precipitate contain the previously unsolved E phase. It has habit plane $\{110\}_{Al}$ and was observed to nucleate exclusively in the distorted regions of the Al matrix.

3.5. Phase mapping by SPED

Fig. 9 shows FFT filtered HAADF-STEM images of the main precipitates along with the corresponding FFTs and matched component patterns from the SPED data decomposition. This is the key information on which the phase decomposition and precipitate statistics extracted from the large SPED scans is based on. As indicated by the red, solid lines that connect the Cu atoms, the L phase in (a) contains a local C atomic configuration. Two orientations of the C phase are shown in (b) and (c) and their characteristic periodicity is highlighted. In (d), a segment of the E phase is shown. The Si-network is indicated by yellow lines in both the FFT patterns and identified component patterns. In the case of the FFTs and PED patterns, only spots corresponding to the 5 nm^{-1} spatial frequencies are connected by the yellow lines. Part of the Si-network is indicated in the images of the disordered L phase (a) and the E phase (d). As discussed earlier, a large part of the Si positions in the E phase is occupied by Cu. The structures presented in the figure are the ones exhibiting well-defined FFTs so that it is possible to identify the corresponding component patterns. Component patterns that did not correspond to any of the main phases were categorised as ' disordered', based on the HAADF-STEM images. Most of the precipitates categorised as disordered contained the Si-network.

Fig. 10 shows the results from the phase identification based on the SPED data for (a) NA20ha and (b) NA20hb. The VDF images are shown for both samples and the red rectangle indicates an area which is enlarged in the remaining images. All the bright spots and streaks correspond to precipitates. The HAADF-STEM investigation

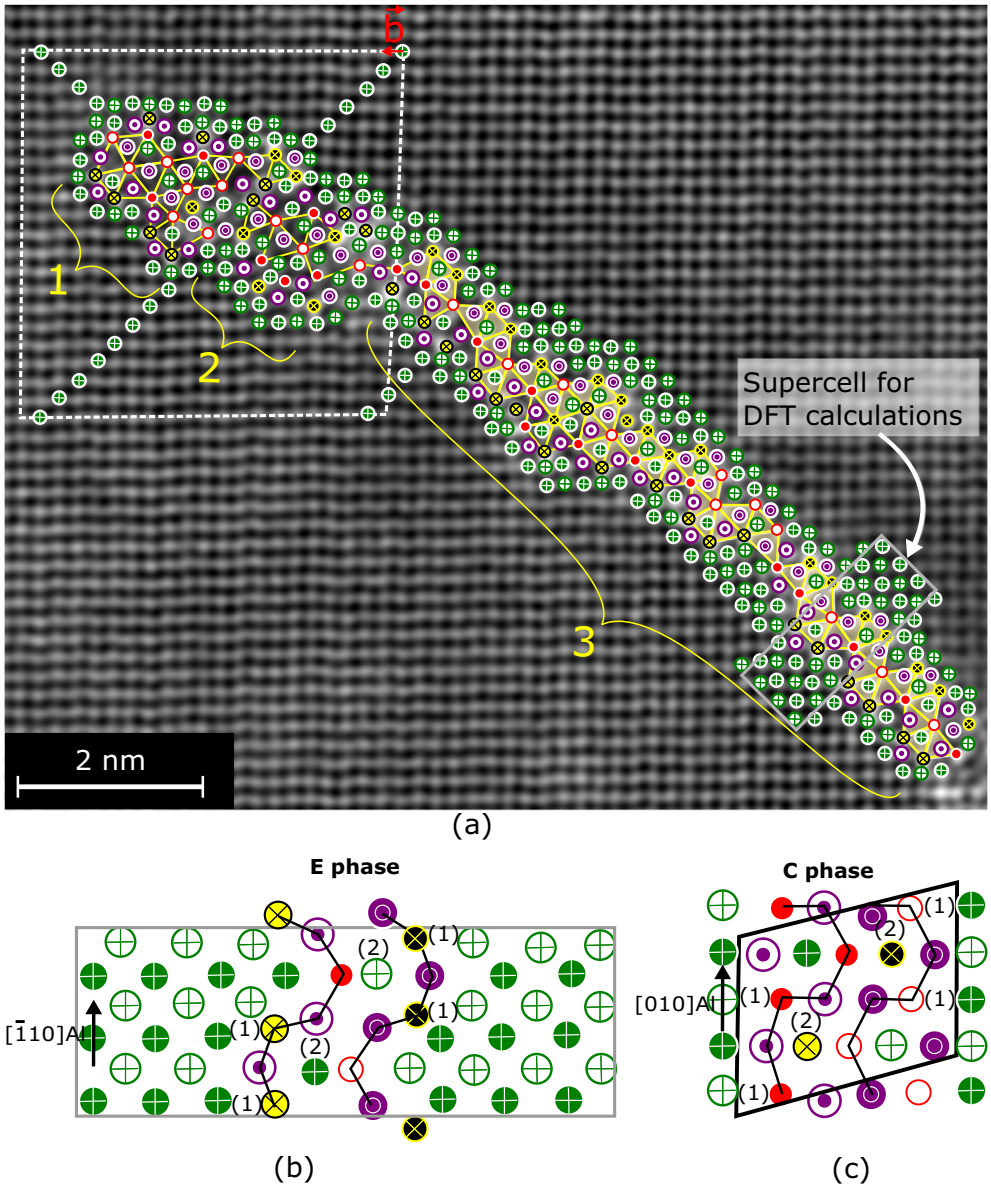

Fig. 8. (a) HAADF-STEM image with atomic overlay of the precipitate in Fig. 7. The legend is shown in Fig. 5. The Si-network is fragmented in three parts, as indicated by the numbers. The $\vec{b}$ indicates the presence of a Burger's vector. In (b), the supercell used for DFT calculations is shown. The black lines enclose the core of the E phase. In (c), the atomic model of the C phase based on the fractional coordinates in Table 3.1 is shown. The black parallelogram and black lines indicate the unit cell and the core of the C phase, respectively. The core of the E phase is derived from the core of the C phase rotated 45 ° from ⟨100⟩ to ⟨110⟩, with Si (1) atomic columns in C being occupied by Cu in E, and the Cu (2) columns in C being occupied by Al in E.

revealed that the precipitates nucleated independently of the dislocation networks were in the range of 2 nm to 6 nm in the main cross-sectional direction. Therefore, all the dots in the VDF images are assumed to correspond to precipitates nucleated homogeneously in the undistorted regions, while the more elongated spots and streaks in the VDF images are assumed to be associated with precipitates nucleated in distorted regions of the Al matrix. The images labelled 'L', 'C', 'E' and 'Disordered' correspond to the sum of the loading

Table 3
Results from DFT calculations on the E phase with three different structure models. The one with the lowest formation enthalpy, $Al_{38}Mg_6Si_2Cu_4$, corresponds to the experimentally observed phase in the present work.

Refined model	Formation enthalpy per atom (eV/atom)	Formation enthalpy/ volume (eV/Å^3)	Refined cell parameters (Å)			Core composition			
			a	*b*	*c*	Al	Mg	Si	Cu
$Al_{38}Mg_6Si_6$	−0.0567	−0.0033	24.400	3.987	8.753	2	6	6	–
$Al_{36}Mg_6Si_6Cu_2$	−0.0671	−0.0040	24.088	4.015	8.636	–	6	6	2
$Al_{38}Mg_6Si_2Cu_4$	−0.0701	−0.0042	24.426	3.980	8.590	2	6	2	4

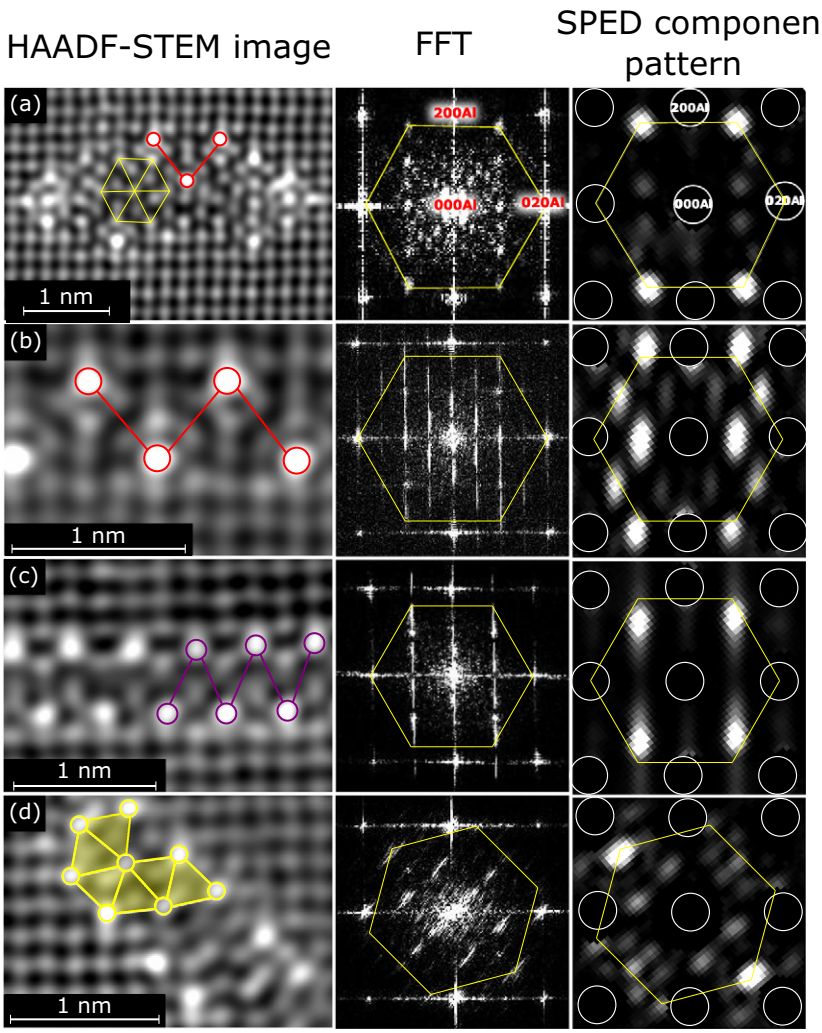

Fig. 9. FFT filtered HAADF-STEM images of the main precipitates types in the pre-deformed samples, the corresponding FFT and component patterns from the SPED data decomposition. The yellow lines indicate the Si-network. In (a), an example of the L phase is shown. The red lines indicate a local arrangement of C in the precipitate. (b) shows a segment of a C phase viewed along $[010]_C$ and the red lines connect Cu atomic columns indicating the 0.81 nm periodicity along $[001]_C$. In (c), a segment of a C phase viewed along $[001]_C$ is shown. The purple lines connect Cu-containing atomic columns, indicating the 0.41 nm periodicity along $[010]_C$. A segment of the E phase is displayed in (d). The component patterns are adjusted for brightness.

maps of the components associated with these phases. As mentioned earlier, some L type precipitates were also nucleated in the distorted regions of the Al matrix. These phases were categorised as disordered, in order to distinguish between heterogeneously and homogeneously nucleated L precipitates.

Note that even though some of the precipitates in the loading maps of the E and the C phase are dot-like, they may still be nucleated in the distorted regions of the Al matrix. As an example, consider the wall-like precipitate of Fig. 6a–c. Short segments of the E phase exist in this structure which will appear as dots in the loading maps. The images labelled ‘ Sum’ correspond to the sum of all loading maps used in the phase identification. By comparing the sum with the corresponding area in the VDF image, it is verified that most the precipitates viewed in the cross-sectional direction are included in the decomposition. The precipitates categorised as disordered in NA20ha are mostly found to be elongated. Based on this, it is believed that this category of precipitates is dominated by the ‘ string-like’ precipitates of Fig. 6d or larger L phases nucleated in distorted regions of the Al matrix. For NA20hb however, the disordered category mostly consists of more ‘ dot-like’ features and it is believed that this category is dominated by precipitates nucleated in the undistorted regions, like the S phase shown in Fig. 6g or the L phase (Fig. 6f).

It should be noted that although SPED has proven to be a powerful technique in visualising precipitates in heavily pre-deformed Al-alloys, the technique is currently limited by the detection system. This is especially true when studying samples with extremely small precipitates with the same habit planes and similar PED patterns, which results in a low signal-to-noise ratio limiting the NMF decomposition. As an example, consider Fig. 9, here the component of the L phase in (a) and the component of the C phase in (b) show some similar features. Due to the low signal-to-noise ratio, the NMF decomposition sometimes produced component patterns consisting of both the L phase and the C phase. This was partly overcome by reducing the number of NMF components so that the output components consisted of either dot-like features or more elongated features without any precipitate vanishing when comparing the sum of all components with the VDF. The HAADF-STEM images showed that the L phase often consisted of small segments of the C phase, which is causing some of the intensity spots in the loading maps of L to also be present in the loading maps of C.

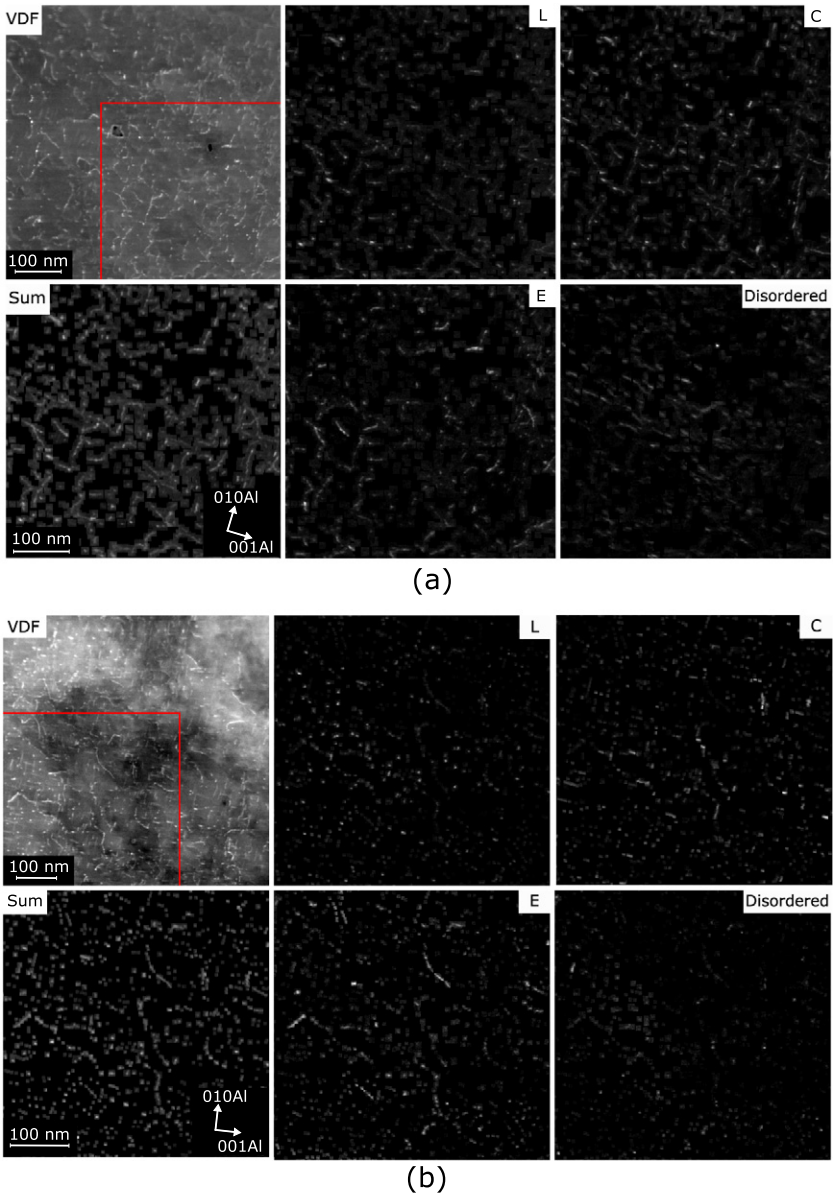

Fig. 10. SPED results including VDF images, loading maps for L, C, E and the disordered category, in addition to the sum of all loading maps used for the phase identification for (a) NA20ha and (b) NA20hb. The red rectangles indicate areas which are enlarged in the loading maps.

3.6. Precipitate fractions

In addition to visualisation of the precipitate distribution, the obtained PED stack was used to approximate the precipitate phase fractions for the two pre-deformed conditions. The estimation of these fractions was based on the approach described in Ref. [26]. The main assumption in this approximation is that the pixel (and hence area) fraction obtained for the different identified phases is similar to the volume fraction of the phases, i.e. $P_f \approx A_f \approx V_f$, where P_f, A_f and V_f denote the pixel-, area- and volume fractions, respectively. This approximation is only valid if the lengths of the different phases observed are nearly equal.

The estimated precipitate phase fractions are shown in the bar chart in Fig. 11. The results indicate that when deforming before NA, the ratio of nucleated L over C+E is larger than when deforming after NA. Based on the previous discussions, this suggests that by deforming after NA (NA20ha), the nucleation of precipitates is more heterogeneous compared to when deformation is conducted prior to NA (NA20hb).

Note that there is an uncertainty associated with the ratios presented in Fig. 11. Different masks in both reciprocal space and real space were tested, and the number of NMF components were varied to see how these factors altered the final precipitate phase fractions. The result showed that the relative ratios of the precipitate phase fractions varied with ±10%, but the conclusion remained unchanged: In NA20ha, the heterogeneous nucleation of precipitates dominated over the homogeneous nucleation of precipitates, and opposite for NA20hb. This conclusion was also supported by the HAADF-STEM images, which showed a larger number ratio of L over C+E in NA20hb than in NA20ha.

3.7. Evaluation of the effect of NA and pre-deformation

It was shown that the sample NA20hn had a precipitate distribution consisting of two main precipitate types: L phases and structural units of GPB-zones. Moreover, it was shown that the introduction of dislocations through cold rolling either before- or after NA caused additional precipitate-types to nucleate in the distorted regions of

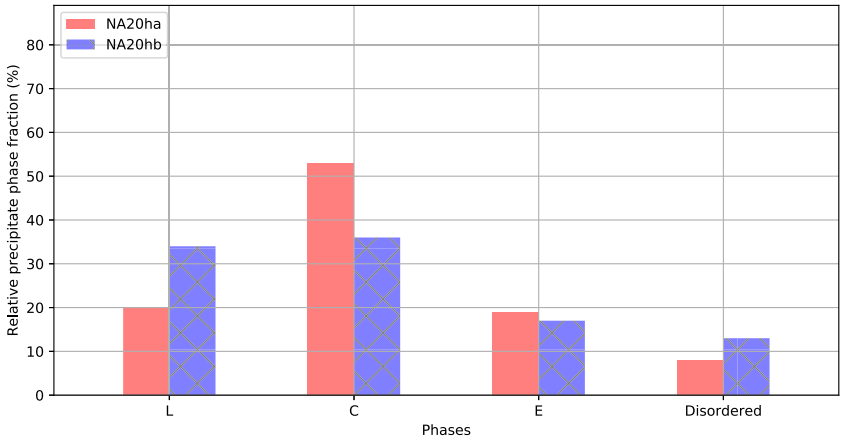

Fig. 11. Bar chart showing the results from the phase quantification by SPED.

the Al matrix. The relative fraction of precipitates nucleated in distorted regions and in undistorted regions were found to be different in the two pre-deformed samples NA20ha and NA20hb. The proposed evolution for NA20ha and NA20hb from SHT throughout the AA treatment is shown in Fig. 12. The schematic is based on the known detrimental effect of NA on the subsequent formation of precipitates during AA, and on the ability of dislocations to provide fast diffusion paths for vacancies and solute segregation leading to preferential precipitation during ageing. Note that the figure's key concepts are exaggerated for clarity and that we assume that the solute uptake in the precipitates are similar for the two conditions.

NA20ha is kept at RT immediately after SHT. The RT storage causes NA clusters to form by the diffusion of solutes using quenched-in vacancies. During the subsequent deformation, the introduced dislocations and NA clusters will interact. It is proposed that some of the NA clusters will dissolve, re-introducing solutes [39,40]. Immediately before the AA treatment, the microstructure therefore consists of NA clusters, solutes and dislocations. During the subsequent AA treatment, the clusters will delay the precipitation in the undistorted regions of the Al matrix, while the solutes will either migrate to the dislocation lines, nucleating heterogeneously as E, C or disordered structures in the distorted regions,

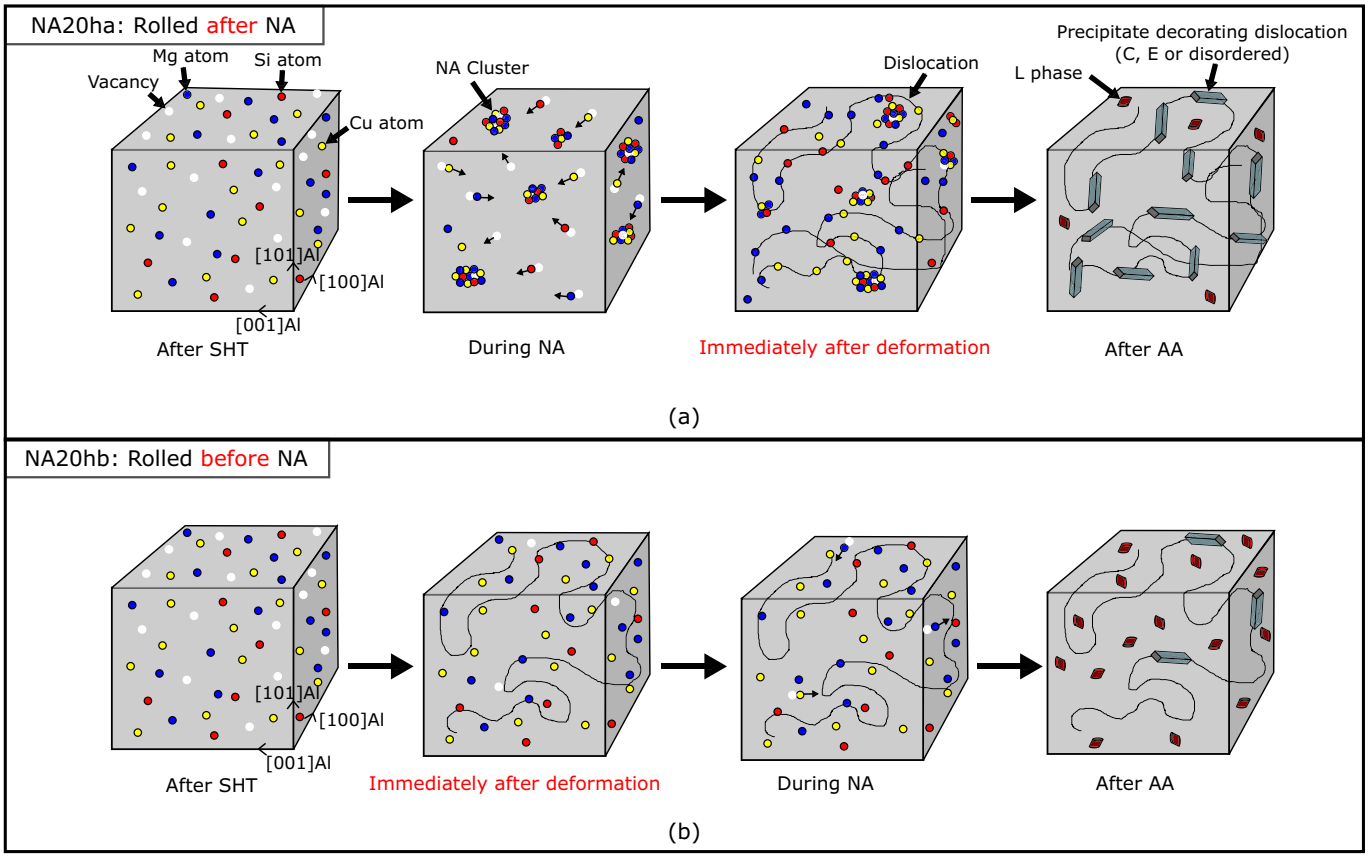

Fig. 12. The suggested microstructure evolution for (a) NA20ha and (b) NA20hb after solution heat treatment.

or nucleate homogeneously as the L phase in the undistorted areas.

NA20hb is deformed prior to NA. In this case, the dislocations are introduced into an environment consisting of a SSSS. During the deformation, a significant proportion of the vacancies will migrate to the dislocations and annihilate. The reduced concentration of vacancies reduces the diffusion of solutes during the subsequent room temperature storage, retaining a solid solution in the undistorted regions of the Al matrix and basically slowing down cluster formation as evidenced by the lower hardness increase during NA in this case, see Fig. 2d. This is believed to be causing the difference in the relative fraction of heterogeneous and homogeneous nucleation in the two samples: The density of NA clusters is lower in NA20hb than NA20ha during the initial stages of the AA treatment. In general, NA clusters forming in alloys with high solute content are associated with delaying the precipitation of hardening phases [41,42] and therefore the lower density of such clusters in NA20hb is causing the relative fraction of homogeneous precipitation to heterogeneous precipitation to be higher than in NA20ha.

It is interesting to note that no β'' precipitates are found in the three conditions investigated in the present work. Since the undeformed sample was found to contain mostly L phases and structural units of GPB-zones, it is believed that the high Cu-content is the reason for this. In a previous work, Marioara et al. [6] demonstrated that for Al-Mg-Si(-Cu) alloys, the L phase is associated with high thermal stability. This is confirmed in the present study, since the hardness of NA20hb, which contains a higher volume fraction of the L phase relative to C and E, decreases slower than the hardness of NA20ha during over-ageing, as seen in the HV-curve in Fig. 2b.

Moreover, it was found that the relative ratio of homogeneously nucleated precipitates to the heterogeneously nucleated precipitates was higher in the softest sample (NA20hb). In undeformed heat-treatable Al alloys, high hardness is associated with a homogeneous distribution of hardening phases. For pre-deformed samples, one has three main contributions to the hardness: both the homogeneously and the heterogeneously nucleated precipitates, in addition to the dislocation density. This work has shown that during a 10 h AA treatment, the NA20hb condition which contained the highest ratio of the hardening L phase to the coarser E- and C-phase after 3 h, was the softest, see Fig. 2b. Thus, precipitate hardening attributed to nucleation of the L phase is not the main hardening mechanism in the heavily pre-deformed samples. It was however shown that during the first three hours of the AA treatment, the hardness increase was most pronounced in NA20hb, see Fig. 2c–d. This is attributed to the higher ratio of the L phase to the coarser phases in this condition. It was also showed that the higher hardness of NA20ha was due to a higher hardness response both during NA and the cold deformation, see Fig. 2c–d. It is believed that the NA clusters present in NA20ha during the deformation is impeding dynamic recovery, making the hardness contribution from the cold working more pronounced in this sample than in NA20hb where the dislocations are introduced into an environment of solid solution.

4. Conclusions

The effect of 80% pre-deformation of an Al-Mg-Si-Cu alloy with high Cu content, applied either before or after a NA treatment for 20 h has been investigated in terms of hardness evolution and precipitate microstructure.

- It was demonstrated that HAADF-STEM in combination with SPED is a powerful tool to investigate precipitation in heavily deformed age-hardening materials.
- For the undeformed condition, two main precipitate types were identified: The L phase and structural units of GPB-zones.
- Three main precipitate types were identified in the deformed conditions, namely L, C and a new precipitate type, called 'E'. The L phase was observed to nucleate both as discrete precipitates on dislocation lines and in undistorted regions away from the dislocation network. C and E were only found at dislocations. C and L have $\{100\}_{Al}$ habit planes.
- The E phase is ordered and has $\{110\}_{Al}$ habit planes. A crystal structure for this phase was proposed here. This structure may be important for the material properties of pre-deformed Al-Mg-Si(-Cu) alloys.
- Deformation after NA enhances heterogeneous precipitation of C and E phases in distorted regions of the Al matrix. On the contrary, deformation applied before NA enhances precipitation of L phase in the undistorted regions. This condition has lower strength due to lower hardness response during NA and cold rolling, but better thermal stability attributed to the higher volume fraction of L phases.

CRediT authorship contribution statement

Elisabeth Thronsen: Conceptualization, Investigation, Data curation, Writing - original draft, Visualization. **Calin D. Marioara:** Conceptualization, Investigation, Writing - review & editing. **Jonas K. Sunde:** Software, Investigation, Writing - review & editing. **Kazuhiro Minakuchi:** Resources, Writing - review & editing, Supervision. **Tetsuya Katsumi:** Resources, Writing - review & editing, Supervision. **Iven Erga:** Investigation, Data curation. **Sigmund J. Andersen:** Formal analysis, Writing - review & editing. **Jesper Friis:** Investigation, Writing - review & editing. **Knut Marthinsen:** Supervision, Writing - review & editing. **Kenji Matsuda:** Resources, Supervision. **Randi Holmestad:** Supervision, Writing - review & editing.

Acknowledgments

The authors would like to acknowledge the Norwegian transmission electron microscopy infrastructure NORTEM (197405). The authors also acknowledge the INTPART project "Norwegian-Japanese Aluminium Alloy Research and Education Collaboration" (249698) funded by the Norwegian Research Council for establishing the collaborations to write this article.

Data availability

The raw/processed data required to reproduce these findings cannot be shared at this time as the data also forms part of an ongoing study.

References

[1] F.J. Humphreys, M. Hatherly, Control of recrystallization, Recrystallization and Related Annealing Phenomena, Elsevier, Oxford, 2004, pp. 469–476. https://doi.org/10.1016/B978-008044164-1/50019-0.
[2] L. Lodgaard, N. Ryum, Precipitation of dispersoids containing Mn and/or Cr in Al-Mg-Si alloys, Mater. Sci. Eng. A 283 (2000) 144–152. https://doi.org/10.1016/S0921-5093(00)00734-6.
[3] C.D. Marioara, S.J. Andersen, H.W. Zandbergen, R. Holmestad, The influence of alloy composition on precipitates of the Al-Mg-Si system, Met. Mater. Trans. A 36A (2005) 691–702. https://doi.org/10.1007/s11661-005-0185-1.
[4] C.D. Marioara, S.J. Andersen, T.N. Stene, H. Hasting, J. Walmsley, A.T.J.V. Helvoort, R. Holmestad, The effect of Cu on precipitation in Al-Mg-Si alloys, Philos. Mag. 87 (2007) 3385–3413. https://doi.org/10.1080/14786430701287377.
[5] H.S. Hasting, A.G. Frøseth, S.J. Andersen, R. Vissers, J.C. Walmsley, C.D. Marioara, F. Danoix, W. Lefebvre, R. Holmestad, Composition of β'' precipitates in Al-Mg-Si alloys by atom probe tomography and first principles calculations, J. Appl. Phys. 106 (123527). (2009) https://doi.org/10.1063/1.3269714.
[6] C.D. Marioara, S.J. Andersen, J. Røyset, O. Reiso, S. Gulbrandsen-Dahl, T. Nicolaisen, I. Opheim, J.F. Helgaker, R. Holmestad, Improving thermal stability in Cu-containing Al-Mg-Si alloys by precipitate optimization, Metall. Mater. Trans. A 45 (2014) 2938–2949. https://doi.org/10.1007/s11661-014-2250-0.

[7] C. Cayron, L. Sagalowicz, O. Beffort, P.A. Buffat, Structural phase transition in Al-Cu-Mg-Si alloys by transmission electron microscopy study on an Al-4 wt% Cu-1 wt% Mg-Ag alloy reinforced by SiC particles, Philos. Mag. A 79 (1999) 2833–2851. https://doi.org/10.1080/01418619908212027.

[8] S.J. Andersen, C.D. Marioara, R. Vissers, A. FrÃÿseth, H.W. Zandbergen, The structural relation between precipitates in Al-Mg-Si alloys, the Al-matrix and diamond silicon, with emphasis on the trigonal phase U1-MgAl2Si2, Mater. Sci. Eng., A 444 (2007) 157–169. https://doi.org/10.1016/j.msea.2006.08.084.

[9] T. Saito, E.A. Mørtsell, S. Wenner, C.D. Marioara, S.J. Andersen, J. Friis, K. Matsuda, R. Holmestad, Atomic structures of precipitates in Al-Mg-Si alloys with small additions of other elements, Adv. Eng. Mater. 20 (1800125). (2018) https://doi.org/10.1002/adem.201800125.

[10] M. Torsæter, F.J.H. Ehlers, C.D. Marioara, S.J. Andersen, R. Holmestad, Applying precipitate-host lattice coherency for compositional determination of precipitates in Al-Mg-Si-Cu alloys, Philos. Mag. 92 (2012) 3833–3856. https://doi.org/10.1080/14786435.2012.693214.

[11] C.D. Marioara, J. Nakamura, K. Matsuda, S.J. Andersen, R. Holmestad, T. Sato, T. Kawabata, S. Ikeno, HAADF-STEM study of β'-type precipitates in an over-aged Al-Mg-Si-Ag alloy, Philos. Mag. 92 (2012) 1149–1158. https://doi.org/10.1080/14786435.2011.642319.

[12] T. Saito, C.D. Marioara, S.J. Andersen, W. Lefebvre, R. Holmestad, Aberration-corrected HAADF-STEM investigations of precipitate structures in Al-Mg-Si alloys with low Cu additions, Philos. Mag. 94 (2014) 520–531. https://doi.org/10.1080/14786435.2013.857051.

[13] C.D. Marioara, A. Lervik, J. GrÃÿnvold, O. Lunder, S. Wenner, T. Furu, R. Holmestad, The correlation between intergranular corrosion resistance and copper content in the precipitate microstructure in an AA6005A alloy, Metall. Mater. Trans. A 49 (2018) 5146–5156. https://doi.org/10.1007/s11661-018-4789-7.

[14] S.J. Andersen, C.D. Marioara, J. Friis, R. Bjørge, Q. Du, I.G. Ringdalen, S. Wenner, E.A. Mørtsell, R. Holmestad, T. Saito, J. Røyset, O. Reiso, Directionality and column arrangement principles of precipitates in Al-Mg-Si-(Cu) and Al-Mg-Cu linked to line defect in Al, The 15th International Conference on Aluminium Alloys, Materials Science Forum, 877, Trans Tech Publications. 2017, pp. 461–470. https://doi.org/10.4028/www.scientific.net/MSF.877.461.

[15] A. Poznak, V. Thole, P. Sanders, The natural aging effect on hardenability in Al-Mg-Si: a complex interaction between composition and heat treatment parameters, Metals 8 (309). (2018) https://doi.org/10.3390/met8050309.

[16] S. Pogatscher, H. Antrekowitsch, T. Ebner, P.J. Uggowitzer, The Role of Co-Clusters in the Artificial Aging of AA6061 and AA6060, Springer International Publishing, Cham, 2016, 415–420. https://doi.org/10.1007/978-3-319-48179-1_70.

[17] M.W. Zandbergen, A. Cerezo, G.D.W. Smith, Study of precipitation in Al-Mg-Si alloys by atom probe tomography II. Influence of Cu additions, Acta Mater. 101 (2015) 149–158. https://doi.org/10.1016/j.actamat.2015.08.018.

[18] M. Werinos, H. Antrekowitsch, T. Ebner, R. Prillhofer, W.A. Curtin, P.J. Uggowitzer, S. Pogatscher, Design strategy for controlled natural aging in Al-Mg-Si alloys, Acta Mater. 118 (2016) 296–305. https://doi.org/10.1016/j.actamat.2016.07.048.

[19] K. Matsuda, S. Shimizu, H. Gamada, Y. Uetani, F. Shinagawa, S. Ikeno, Effect of deformation on the precipitates in Al-Mg_2Si alloys containing silicon in excess, J. Soc. Mater. Sci. Japan 48 (1999) 385–390. https://doi.org/10.2472/jsms.48.10.

[20] K. Matsuda, H. Gamada, Y. Uetani, S. Rengakuji, F. Shinagawa, S. Ikeno, Specific precipitates in Al-Mg_2Si alloys aged after deformation, J. Jpn. Inst. Met. 48 (1998) 471–475. https://doi.org/10.2464/jilm.48.471.

[21] K. Teichmann, C.D. Marioara, S.J. Andersen, K.O. Pedersen, S. Gulbrandsen-Dahl, M. Kolar, R. Holmestad, K. Marthinsen, HRTEM study of the effect of deformation on the early precipitation behaviour in an AA6060 Al-Mg-Si alloy, Philos. Mag. 91 (2011) 3744–3754. https://doi.org/10.1080/14786435.2011.593577.

[22] K. Teichmann, C.D. Marioara, S.J. Andersen, K. Marthinsen, The effect of preaging deformation on the precipitation behavior of an Al-Mg-Si alloy, Metall. Mater. Trans. A 43 (2012) 4006–4014. https://doi.org/10.1007/s11661-012-1235-0.

[23] S. Jin, T. Ngai, L. Li, S. Jia, T. Zhai, D. Ke, Aging response and precipitation behavior after 5% pre-deformation of an Al-Mg-Si-Cu alloy, Materials 11 (1422). (2018) https://doi.org/10.3390/ma11081422.

[24] D. Yin, Q. Xiao, Y. Chen, H. Liu, D. Yi, B. Wang, S. Pan, Effect of natural ageing and pre-straining on the hardening behaviour and microstructural response during artificial ageing of an Al-Mg-Si-Cu alloy, Mater. Des. 95 (2016) 329–339. https://doi.org/10.1016/j.matdes.2016.01.119.

[25] J.K. Sunde, Ø. Paulsen, S. Wenner, R. Holmestad, Precipitate statistics in an Al-Mg-Si-Cu alloy from scanning precession electron diffraction data, J. Phys. Conf. Ser. 902 (012022). (2017) https://doi.org/10.1088/1742-6596/902/1/012022.

[26] J.K. Sunde, C.D. Marioara, A.T.J. van Helvoort, R. Holmestad, The evolution of precipitate crystal structures in an Al-Mg-Si(-Cu) alloy studied by a combined HAADF-STEM and SPED approach, Mater. Charact. 142 (2018) 458–469. https://doi.org/10.1016/j.matchar.2018.05.031.

[27] J.S. Barnard, D.N. Johnstone, P.A. Midgley, High-resolution scanning precession electron diffraction: alignment and spatial resolution, Ultramicroscopy 1 (2017) 79–88. https://doi.org/10.1016/j.ultramic.2016.12.018.

[28] G. Kresse, J. Hafner, Ab initio molecular dynamics for liquid metals, Phys. Rev. B 47 (1993) 558–561. https://doi.org/10.1016/0022-3093(95)00355-X.

[29] G. Kresse, J. Furthmüller, Efficiency of ab-initio total energy calculations for metals and semiconductors using a plane-wave basis set, Comput. Mater. Sci. 6 (1996) 15–50. https://doi.org/10.1016/0927-0256(96)00008-0.

[30] J.P. Perdew, K. Burke, M. Ernzerhof, Generalized gradient approximation made simple, Phys. Rev. Lett. 77 (1996) 3865–3868. https://doi.org/10.1103/PhysRevLett.77.3865.

[31] C.D. Marioara, W. Lefebvre, S.J. Andersen, J. Friis, Atomic structure of hardening precipitates in an Al-Mg-Zn-Cu alloy determined by HAADF-STEM and first-principles calculations: relation to $\eta - MgZn_2$, J. Mater. Sci. 48 (3638). (2013) https://doi.org/10.1007/s10853-013-7158-3.

[32] F. de La Peña, V.T. Fauske, P. Burdet, E. Prestat, P. Jokubauskas, M. Nord, T. Ostasevicius, K.E. MacArthur, M. Sarahan, D.N. Johnstone, J. Taillon, A. Eljarrat, V. Migunov, J. Caron, T. Furnival, S. Mazzucco, T. Aarholt, M. Walls, T. Slater, F. Winkler, B. Martineau, G. Donval, R. McLeod, E.R. Hoglund, I. Alxneit, I. Hjorth, T. Henninen, L.F. Zagonel, A. Garmannslund, A. Skorikov, Hyperspy/Hyperspy V1.4.1, 2018. https://doi.org/10.5281/zenodo.1469364.

[33] A.S. Eggeman, R. Krakow, P.A. Midgley, Scanning precession electron tomography for three-dimensional nanoscale orientation imaging and crystallographic analysis, Nat. Commun. 6 (7267). (2015) https://doi.org/10.1038/ncomms8267.

[34] T. Masuda, Y. Takaki, T. Sakurai, S. Hirosawa, Combined effect of pre-straining and pre-aging on bake-hardening behavior of an Al-0.6 mass%Mg-1.0 mass%Si alloy, Mater. Trans. 51 (2010) 325–332. https://doi.org/10.2320/matertrans.L-M2009831.

[35] Y. Birol, Pre-straining to improve the bake hardening response of a twin-roll cast Al-Mg-Si alloy, Scr. Mater. 52 (2005) 169–173. https://doi.org/10.1016/j.scriptamat.2004.10.001.

[36] L. Kovarik, S.A. Court, H.L. Fraser, M.J. Mills, GPB zones and composite GPB/GPBII zones in Al-Cu-Mg alloys, Acta Mater. 56 (2008) 4804–4815. https://doi.org/10.1016/j.actamat.2008.05.042.

[37] M. Mihara, C.D. Marioara, S.J. Andersen, R. Holmestad, E. Kobayashi, T. Sato, Precipitation in an Al-Mg-Cu alloy and the effect of a low amount of Ag, Mater. Sci. Eng. A 658 (2016) 91–98. https://doi.org/10.1016/j.msea.2016.01.087.

[38] T. Saito, S. Muraishi, C.D. Marioara, S.J. Andersen, J. Røyset, R. Holmestad, The effects of low Cu additions and predeformation on the precipitation in a 6060 Al-Mg-Si alloy, Metall. Mater. Trans. A 44 (2013) 4124–4135. https://doi.org/10.1007/s11661-013-1754-3.

[39] Z. Wang, H. Li, F. Miao, B. Fang, R. Song, Z. Zheng, Improving the strength and ductility of Al-Mg-Si-Cu alloys by a novel thermo-mechanical treatment, Mater. Sci. Eng., A 607 (2014) 313–317. https://doi.org/10.1016/j.msea.2014.04.009.

[40] A. Serizawa, T. Sato, W.J. Poole, The characterization of dislocation-nanocluster interactions in Al-Mg-Si(-Cu/Ag) alloys, Philos. Mag. Lett. 90 (2010) 279–287. https://doi.org/10.1080/09500831003633231.

[41] C.D. Marioara, S.J. Andersen, J. Jansen, H.W. Zandbergen, The influence of temperature and storage time at RT on nucleation of the β'' phase in a 6082 Al-Mg-Si alloy, Acta Mater. 51 (2003) 789–796. https://doi.org/10.1016/S1359-6454(02)00470-6.

[42] F.A. Martinsen, F.J.H. Ehlers, M. Torsæter, R. Holmestad, Reversal of the negative natural aging effect in Al-Mg-Si alloys, Acta Mater. 60 (2012) 6091–6101. https://doi.org/10.1016/j.actamat.2012.07.047.